

# Opto-Electronic Science

CN 51-1800/O4 ISSN 2097-0382 (Print) ISSN 2097-4000 (Online)

## Tailoring temperature response for a multimode fiber

Han Gao, Haifeng Hu and Qiwen Zhan

**Citation:** Gao H, Hu HF, Zhan QW. Tailoring temperature response for a multimode fiber. *Opto-Electron Sci* 4, 240004 (2025).

<https://doi.org/10.29026/oes.2025.240004>

Received: 26 January 2024; Accepted: 13 May 2024; Published online: 20 August 2024

## Related articles

### Mode-locked fiber laser with multimode fiber as saturable absorber

Hong Yao, Zhang Jing, Ji Haiying, Sun Mengru, Wang Tianshu

*Opto-Electronic Engineering* 2021 **48**, 200362 doi: [10.12086/oe.2021.200362](https://doi.org/10.12086/oe.2021.200362)

### Seeing at a distance with multicore fibers

Haogong Feng, Xi Chen, Runze Zhu, Yifeng Xiong, Ye Chen, Yanqing Lu, Fei Xu

*Opto-Electronic Advances* 2024 **7**, 230202 doi: [10.29026/oea.2024.230202](https://doi.org/10.29026/oea.2024.230202)

### Refractive index insensitive two parameter sensor based on dual mode LPEG

Wang Xiangyu, Qiao Xueguang, Yu Dakuan

*Opto-Electronic Engineering* 2021 **48**, 200247 doi: [10.12086/oe.2021.200247](https://doi.org/10.12086/oe.2021.200247)

### A FOG start-up drift compensation method at full temperatures before and after compensation comparison

Yao Leishan, Zhou Yilan, Zhao Shuai, Huang Tengchao, Che Shuangliang

*Opto-Electronic Engineering* 2024 **51**, 240033 doi: [10.12086/oe.2024.240033](https://doi.org/10.12086/oe.2024.240033)

More related article in Opto-Electronic Journals Group website 



Opto-Electronic  
Science

<http://www.oejournal.org/oes>



 OE\_Journal



Website

DOI: [10.29026/oes.2025.240004](https://doi.org/10.29026/oes.2025.240004)

# Tailoring temperature response for a multimode fiber

Han Gao<sup>1,2</sup>, Haifeng Hu<sup>1,3,4\*</sup> and Qiwen Zhan<sup>1,3,4\*</sup>

This work introduces special states for light in multimode fibers featuring strongly enhanced or reduced correlations between output fields in the presence of environmental temperature fluctuations. Using experimentally measured multi-temperature transmission matrix, a set of temperature principal modes that exhibit resilience to disturbances caused by temperature fluctuations can be generated. Reversing this concept also allows the construction of temperature anti-principal modes, with output profiles more susceptible to temperature influences than the unmodulated wavefront. Despite changes in the length of the multimode fiber within the temperature-fluctuating region, the proposed approach remains capable of robustly controlling the temperature response within the fiber. To illustrate the practicality of the proposed special state, a learning-empowered fiber specklegram temperature sensor based on temperature anti-principal mode sensitization is proposed. This sensor exhibits outstanding superiority over traditional approaches in terms of resolution and accuracy. These novel states are anticipated to have wide-ranging applications in fiber communication, sensing, imaging, and spectroscopy, and serve as a source of inspiration for the discovery of other novel states.

**Keywords:** multimode fiber; principal mode; wavefront shaping; optical fiber sensor; temperature response

Gao H, Hu HF, Zhan QW. Tailoring temperature response for a multimode fiber. *Opto-Electron Sci* 4, 240004 (2025).

## Introduction

Multimode fiber (MMF) is an intricate and indispensable system that plays a pivotal role in a diverse array of applications, ranging from optical transmission<sup>1-5</sup>, imaging<sup>6-10</sup>, and sensing<sup>11-15</sup>, to high-power laser<sup>16,17</sup> and optical amplifier<sup>18,19</sup>. Across all these diverse application domains, the ability of MMF to carry a large number of transverse optical modes is both a critical feature and a significant challenge. Compared to single-mode fiber (SMF), which can only support a single transverse optical mode, MMF exhibits significantly enhanced information-carrying capacity. Moreover, the structural characteristics of MMF enable fiber-based lasers and amplifiers to operate at high power levels. However, mode disper-

sion, unavoidable random mixing between modes with different propagation constants, intrinsic defects of the fiber, and disorder induced by external perturbations can cause significant distortion of the optical signal propagating through the MMF. After injecting coherent light into MMF, a seemingly random and chaotic pattern with bright and dark spots, called speckle pattern, can be observed at the output. Understanding and manipulating this distortion in MMFs remains an important challenge for applications in optical telecommunications, endoscopic imaging, and micro-manipulation.

Recently, transmission matrix (TM) has become a powerful tool for characterizing and controlling the propagation of light in complex but deterministic optical

<sup>1</sup>School of Optical-Electrical and Computer Engineering, University of Shanghai for Science and Technology, Shanghai 200093, China; <sup>2</sup>Institute of Modern Optics, Nankai University, Tianjin 300350, China; <sup>3</sup>Zhangjiang Laboratory, 100 Haik Road, Shanghai 201204, China; <sup>4</sup>Shanghai Key Lab of Modern Optical System, University of Shanghai for Science and Technology, Shanghai 200093, China.

\*Correspondence: HF Hu, E-mail: [hfh@usst.edu.cn](mailto:hfh@usst.edu.cn); QW Zhan, E-mail: [qwzhan@usst.edu.cn](mailto:qwzhan@usst.edu.cn)

Received: 26 January 2024; Accepted: 13 May 2024; Published online: 20 August 2024



**Open Access** This article is licensed under a Creative Commons Attribution 4.0 International License.

To view a copy of this license, visit <http://creativecommons.org/licenses/by/4.0/>.

© The Author(s) 2025. Published by Institute of Optics and Electronics, Chinese Academy of Sciences.

linear systems<sup>20</sup>. The TM was originally proposed and demonstrated in the context of scattering media, and it is obtained by measuring the linear relationship between optical wavefronts on the incident plane and observation plane. The conjugate and time-reversal properties of the TM enable convenient manipulation of the output optical field of scattering media<sup>21–23</sup> or imaging<sup>24–26</sup>. Subsequently, this concept was transferred to MMFs, which further facilitated the development of various applications, including endoscopic imaging<sup>27</sup>, micromanipulation<sup>28</sup>, quantum information processing<sup>29</sup>. However, the use of TM is not capable of entirely describe the transmission properties of MMF in a dynamic state<sup>30</sup>. In fact, one of the major challenges in the practical application of MMF is not only understanding the impact of external disturbance, but also completely avoiding it. In recent times, the time-delay operator introduced by Wigner and Smith<sup>31,32</sup> in quantum mechanics has garnered significant interest among researchers. Simultaneously, with the advancement of wavefront shaping technology and devices, detecting a single Wigner-Smith eigenstate in optics has become possible. By extending the concept of polarization mode in single-mode fiber, the Wigner-Smith eigenstate, also referred to as the principal mode (PM) in MMFs, has emerged as a promising strategy to mitigate mode dispersion<sup>33–36</sup>. Through this approach, ultra-short light pulses can be transmitted through MMFs with unprecedented fidelity in the temporal dimension. In 2015, the existence of the PM in MMFs was experimentally validated for the first time by J. Carpenter et al.<sup>33</sup>, who demonstrated its superiority over the Laguerre-Gaussian mode in different types of MMFs. This groundbreaking achievement confirmed the viability of the Wigner-Smith eigenstate as a powerful tool for suppressing mode dispersion and improving the performance of optical communication systems. Due to the universality of the PM concept, researchers have realized that by employing the generalized Wigner-Smith operator, the search for channels that are insensitive to external disturbance can be extended beyond the incident light frequency to other parameters<sup>30</sup>. However, research on utilizing the generalized Wigner-Smith operator to search for novel and special states in MMF remains scarce.

In this work, we utilized a generalized Wigner-Smith operator constructed according to the multi-temperature transmission matrix of MMF to generate special optical states called temperature principal modes, using

wavefront shaping techniques. Compared with the unmodulated incident beams, the temperature principal mode exhibits greater resistance to temperature-induced distortions of output speckle patterns. Furthermore, by reversing the concept, our approach can also be employed to generate temperature anti-principal mode with extremely narrow temperature bandwidth, which have potential applications in the field of optical fiber sensing. Experimental results have demonstrated that the learning-empowered fiber specklegram temperature sensor sensitized by the temperature anti-principal mode is significantly superior to traditional solutions in terms of resolution and demodulation accuracy. The proposed approach in this work holds promise for a wide range of applications in imaging, sensing, and communication, and is expected to serve as a universal framework for promoting to other multimode waveguides.

## Methods

### Temperature principal modes and anti-principal modes

The fidelity between the transmission matrix of the perturbed fiber and the reference matrix for the unperturbed configuration decreases quickly as the temperature  $\Delta T$  increases. While temperature fluctuations can alter transmission characteristics, our objective is to identify a set of channels minimally affected by fluctuations in ambient temperature, which are referred to as the temperature principal modes. The temperature principal modes refer to a set of optical channels that exhibit remarkable resistance to temperature-induced distortions. Compared to unmodulated wavefronts, the temperature principal modes can enable the output field of a MMF to maintain high correlation over a wider temperature range. Here, we introduce a method based on the Wigner-Smith operator to calculate the temperature principal mode and temperature anti-principal mode in a MMF. In optical fibers, the Wigner-Smith operator  $Q$  can be expressed as<sup>35</sup>:

$$Q = -iU^{-1}(T_0) \frac{U(T) - U(T_0)}{T - T_0}, \quad (1)$$

where  $U$  is the transmission matrix. Temperature principal modes  $\phi$  are the eigenstate of the Wigner-Smith operator  $Q$ .

To provide a quantitative assessment, we describe the suppressive effect of the temperature principal mode on temperature-induced distortions by calculating the

correlation function  $C$ . The correlation function  $C$  can be expressed as<sup>35</sup>:

$$C(\Delta T \equiv T - T_0) \equiv |\psi^\dagger(T_0) \cdot \psi(T)|, \quad (2)$$

where  $\psi(T)$  represents the normalized output optical field under the temperature of  $T$ . As the value of  $C$  approaches 1, the correlation between the output optical fields becomes higher.

To further enhance the bandwidth of the temperature principal mode, a loss function  $\Gamma$  has been introduced. The loss function  $\Gamma$  can be expressed as<sup>36</sup>:

$$\begin{aligned} \Gamma(\phi) &= \int dT [1 - C(\Delta T)^2] \\ &= \int dT \left[ 1 - \frac{|\psi^\dagger(T) \cdot \psi(T_0)|^2}{|\psi(T)|^2 |\psi(T_0)|^2} \right]. \end{aligned} \quad (3)$$

It can be observed that by minimizing the value of the loss function  $\Gamma$ , which can be achieved through gradient algorithms, the temperature principal mode with optimized bandwidth can be obtained. When applying optimization algorithms to minimize the loss function, it is recommended to use the temperature principal mode obtained through Eq. (1) as the initial value for the optimization loop.

The temperature anti-principal modes are a set of optical channels that are more sensitive to temperature-induced distortion. Compared to the unmodulated wavefront (e.g. Gaussian beam), the speckle patterns generated by the temperature anti-principal mode exhibit a higher degree of decorrelation with each other under varying temperature conditions. Unlike the process for obtaining the optimized temperature principal mode, the temperature anti-principal mode can be easily obtained by maximizing the loss function  $\Gamma$  described in Eq. (3)<sup>36</sup>.

### Experimental setup

As shown in Fig. 1, the continuous wave output of the laser (Santec TSL-550) is collimated and expanded before being split into two arms by a beam splitter (BS1). The linewidth and operating wavelength of the laser used in this experiment are 200 kHz and 1550 nm, respectively. The light in one arm is modulated using a spatial light modulator (SLM, HOLOEYE, GAEA-2, pixel size:  $3.74 \mu\text{m} \times 3.74 \mu\text{m}$ , resolution:  $4160 \times 2464$ ) and then projected onto the proximal end face of a 1 m long multimode optical fiber (MMF,  $62.5/125 \mu\text{m}$  core/cladding diameters). In this study, the multimode fiber supports approximately 390 modes, and the signal light is modulated using  $1500 \times 1500$  pixels at the center of the SLM. The two lens-

es (L3 and L4) used in the experiment are both manufactured by Thorlabs, with a model designation of LA1509-C and a focal length of 100 mm. The output field of the fiber is acquired by means of a microscope objective (OBJ2, Nikon, CFI40X,  $40\times$ ,  $NA=0.75$ ) and subsequently superimposed with the light in the reference arm at the second beam splitter (BS2). The interference fringes are generated by inducing a phase tilt between the two wavefronts through the use of the beam splitter (BS2). The interference pattern was recorded with a camera (CCD, Xenics, Bobcat 640 GigE, 16-bit). Subsequently, the amplitude and phase distributions of the output field were extracted in momentum space. To obtain the transmission matrices of the optical fiber at different temperatures, the fiber was heated using a hot plate. The multimode fiber used in this work has a coating layer. Therefore, to ensure accuracy and minimize potential errors, we waited for ten minutes after each temperature change before initiating data collection. The overall dimensions of the experimental setup are  $95 \text{ cm} \times 70 \text{ cm}$ .

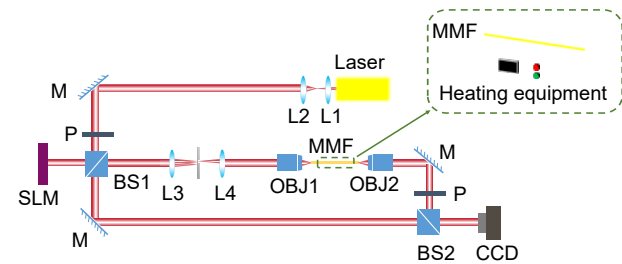


**Fig. 1 | Schematics of the experimental setup.** OBJ: microscopic objective (OBJ1:  $20\times$ ,  $NA$  (numerical aperture) = 0.40; OBJ2:  $40\times$ ,  $NA=0.75$ ); CCD: charge-coupled device camera; MMF: multimode fiber; SLM: spatial light modulator; P: polarizer; M: mirror; BS: beam splitter; L: lens.

### Results

To construct the Wigner-Smith operator, we employed the interferometer illustrated in Fig. 1 to measure the field transmission matrix of a MMF across various temperatures. The wavefront of the optical field is modulated by a SLM in the fiber arm and subsequently projected onto the proximal face of MMF. The resultant interferogram, formed by combining the output field of the fiber with a reference beam, is analyzed to extract the amplitude and phase distribution of the transmitted field through the fiber. To reduce noise, a filtering process was applied by discarding the eigenchannels with very high loss in the measured transmission matrices<sup>36</sup>. Specifically, the channels with eigenvalues less than 1% of the



maximum eigenvalue in the transmission matrix were discarded. The reason for conducting this filtering can be attributed to the fact that eigenchannels with smaller eigenvalues will introduce substantial errors, leading to the computed Wigner-Smith operator being highly sensitive to noise and system errors. Therefore, despite truncating the transmission matrix and discarding some of its transmission characteristics, the filtering process mitigates the ill-conditioning of the transmission matrix and enhances the robustness of the Wigner-Smith operator to disturbances. In this experiment, a total of 80 eigenchannels were retained. The temperature principal mode and temperature anti-principal mode corresponding input states were generated using SLM and launched into the fiber for propagation. As this work employs a phase-only modulation type of SLM, it is necessary to use complex-phase encoding techniques to convert the phase-only holograms into complex functions with both amplitude and phase modulation<sup>37</sup>. It should be noted that this work focuses only on the study of one linear polarization state of the input and output light. Due to the distortion that occurs as the input light propagates through the MMF, some of the input light is converted to another polarization state, resulting in the loss of this information at the output. Therefore, even in the absence of intrinsic losses, the measured transmission matrix is non-unitary and can be regarded as a subset of the full transmission matrix that includes both polarizations. Despite this, it is still possible to obtain a Wigner-Smith operator corresponding to one polarization from the partial transmission matrix<sup>34</sup>, and its eigenstates can be used to manipulate the response of one polarization component of the output field to temperature-induced distortion. Currently, the calibration time for the temperature principal modes and anti-principal modes is approximately ten minutes, with most of the time spent on calibrating the multi-temperature transmission matrix. Using wavefront shaping devices with faster modulation rates, such as DMD (digital micromirror device), can significantly improve the calibration speed by two orders of magnitude<sup>38</sup>. Additionally, employing compressive sensing algorithms enables the reconstruction of the complete transmission matrix under undersampling conditions<sup>39</sup>, further enhancing the real-time feasibility of the proposed approach.

Computer-generated phase holograms were loaded onto a SLM, and temperature principal modes and temperature anti-principal modes were constructed through

amplitude and phase modulation. Corresponding output fields were recorded as the environmental temperature was scanned, and the correlation between the output-field patterns was calculated using Eq. (2). The temperature bandwidth  $\delta T$  is defined as the temperature change required to induce decorrelation of the output optical field and can be expressed as:

$$C(\delta T/2) = C(0)/2. \quad (4)$$

Figure 2 illustrates the relationship between the correlation of the output field and temperature variation, represented by the red solid line for the temperature principal mode, the green solid line for the temperature anti-principal mode, and the blue solid line for the unmodulated wavefront. When the length of the MMF in the temperature fluctuation region is 10 cm, the temperature bandwidth of the unmodulated wavefront is 40.6 °C, while the temperature bandwidths of the temperature principal mode and temperature anti-principal mode are 57.4 °C and 27.4 °C, respectively. Compared with the unmodulated wavefront, the temperature bandwidth can be increased by about 40% using the temperature principal mode. In contrast, the temperature anti-principal mode reduces the temperature bandwidth to 67% of the unmodulated wavefront.

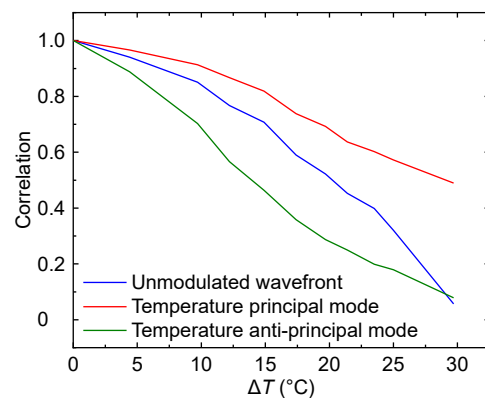


**Fig. 2 |** Calculated correlation function for output signals of the unmodulated wavefront (blue solid line), the temperature principal mode (red solid line) and the temperature anti-principal mode (green solid line).

Figure 3 provides a more intuitive demonstration of the manipulative effects on temperature response in MMF, where the top, middle, and bottom rows respectively represent the intensity distribution of the output field corresponding to the temperature principal mode, the temperature anti-principal mode, and the unmodulated wavefront. The middle panel of Fig. 3 represents

the initial state, while the left and right panels respectively depict the intensity distribution of the output field at the distal end of the fiber under temperature fluctuations of  $-10\text{ }^{\circ}\text{C}$  and  $10\text{ }^{\circ}\text{C}$ . It can be visually and intuitively observed that the scheme described in this work can effectively manipulate the temperature response in MMF.

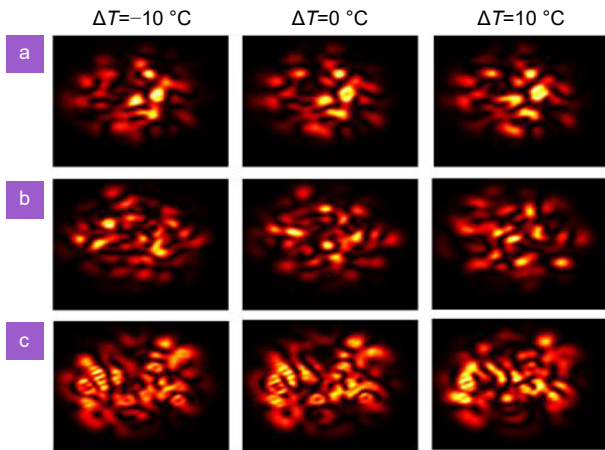


**Fig. 3 |** Recorded intensity profiles of (a) temperature principal mode (top row), (b) temperature anti-principal mode (middle row) and (c) unmodulated wavefront (bottom row) at the distal end of the fiber.

To explore the applicability of the proposed scheme, we further investigated scenarios with fiber lengths of 20 cm, 30 cm, 40 cm, and 50 cm in regions of temperature fluctuations. By recalibration, the proposed approach remains robust as the length of the fiber in the path increases. Figure 4 displays the normalized bandwidths of the temperature principal mode and temperature anti-principal mode, normalized by the temperature bandwidth of unmodulated wavefront. When the lengths of the fiber in the temperature fluctuation region are 10 cm, 20 cm, 30 cm, 40 cm, and 50 cm, the normalized bandwidths of the temperature principal mode are 1.41, 1.45, 1.43, 1.46 and 1.44, while the normalized bandwidths of the temperature anti-principal mode are 0.67, 0.65, 0.64, 0.67 and 0.66, respectively. Despite the change in fiber length, the approach proposed in this work can still robustly manipulate the temperature response of MMF.

To compare the effects of heating environments on the principal modes, we utilized both water bath heating and hot plate heating methods to generate the principal modes. When the length of the fiber in the temperature fluctuation region is 30 cm, the normalized bandwidths of the temperature principal modes generated by the water bath heating method and the hotplate heating method are 1.43 and 1.45, respectively, while the normal-

ized bandwidths of the anti-principal modes are 0.64 and 0.62, respectively. The experimental results reveal that, with uniform temperature distribution inside the optical fiber ensured, the bandwidths of the principal and anti-principal modes obtained through both heating methods are similar.

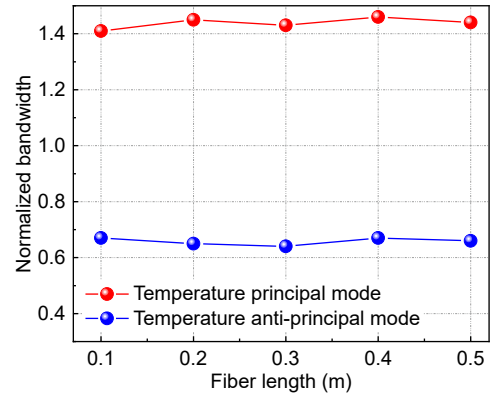


**Fig. 4 |** Normalized bandwidth of the temperature principal mode and the temperature anti-principal mode for different fiber length.

Temperature principal mode can suppress temperature-induced distortions, which has potential applications in fields such as fiber optic spectrometers, imaging, and communication. On the other hand, the temperature anti-principal mode can enhance the response of fiber optic to external perturbations, and therefore holds promise for advancing the field of fiber optic sensing. Fiber optic sensors have been widely used in various fields due to their small size, high sensitivity, and resistance to electromagnetic interference. In the reported works, fiber specklegram sensors are considered as a promising candidate for widely applicable fiber sensing technologies due to their advantages of not requiring expensive sensor interrogation schemes or complex fabrication processes<sup>40</sup>. Fiber specklegram sensor is devoted to analyzing the statistical information of the speckle pattern generated at the distal end of the fiber, and predicting the sensing parameter based on the correlation coefficient between the speckle patterns. Therefore, the sensitivity of fiber specklegram sensor relies on the distortion induced by external disturbances. Currently, methods to increase the sensitivity of fiber optic temperature sensors, such as using specialty fibers<sup>41,42</sup>, coating<sup>43</sup> or filling<sup>11</sup> with sensitive materials, or designing and fabricating special sensing structures<sup>44,45</sup>, often compromise the robustness of the fiber optic structure or increase the time and experimental effort required, which is not conducive to practical applications. The temperature

anti-principal mode can enhance the temperature-induced distortion in optical fibers, thereby improving the performance of fiber specklegram temperature sensors without compromising the robustness of fiber structures or requiring complex fabrication processes. To validate the feasibility, we proposed a fiber specklegram temperature sensor enhanced by the temperature anti-principal mode. In traditional fiber specklegram sensing schemes, various techniques such as normalized inner-product coefficient (NIPC)<sup>46</sup>, zero mean normalized cross-correlation coefficient (ZNCC)<sup>40</sup>, and morphological image processing<sup>47</sup> have been proposed to fit the relationship between speckle patterns and sensing parameters. However, these techniques often focus on analyzing the statistical information of speckle patterns and do not fully utilize the abundant information carried by many fiber modes. Hence, these methods have limitations in fully capturing the evolution of speckle patterns under specific perturbations. Deep learning has emerged as a prominent research field in recent years, and its ability to mine and learn the complex relationship between speckle patterns and sensing parameters has resulted in a high-performance sensing signal demodulation solution<sup>48</sup>. The learning empowered fiber specklegram temperature sensing scheme based on temperature anti-principal mode sensitization is shown in Fig. 5. The temperature anti-principal mode was calibrated using the aforementioned method, and then speckle patterns corresponding to the temperature anti-principal mode were collected at different temperatures to create a dataset. A deep learning model was then employed to learn the relationship between speckle patterns and temperature. The trained model is capable of directly predicting the corresponding temperature value based on the speckle pattern collected at the distal end of the fiber.

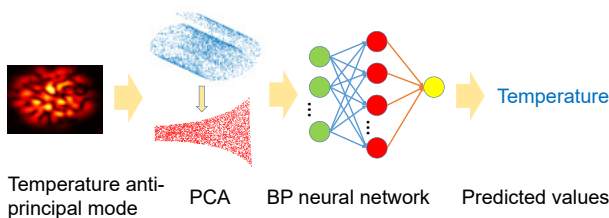


**Fig. 5 | Overview of learning empowered fiber specklegram temperature sensing schemes based on temperature anti-principal mode sensitization.**

As a data-driven model, deep learning hinges on the solution space offered by the dataset to mine and comprehend the relationship between speckle patterns and

sensing parameters. Therefore, the first step is to collect a large number of raw samples containing various configurations. In this work, the length of the multimode fiber in the sensing area is 10 cm, and the temperature surrounding the fiber is increased from 30 °C to 45 °C in steps of 1 °C. In this study, the temperature anti-principal mode was calculated and utilized as the incident wavefront. A total of 50 images were collected for each temperature group, with the collection process repeated four times to ensure data diversity. Consequently, a total of 16 different configurations were gathered, and each configuration was composed of 200 speckle patterns. The second step involved transforming the collected data into a dataset. To evaluate the predictive performance of the trained model on both learned and unlearned configurations, two different test sets were utilized, enabling a more accurate assessment of the generalization ability of the model. Specifically, 10 sets were randomly selected from the collected 16 groups and divided into Group B, while the remaining samples were assigned to Group A. Within Group A, the speckle patterns were split equally into training set A and testing set A, with a 1 : 1 ratio. The samples in Group B were designated as testing set B. The training set A was utilized to provide a solution space for the neural network to learn the evolution pattern between speckle patterns and temperature. The task of testing set A is to characterize the generalization ability of the trained model to the learned configurations. Testing set B, on the other hand, comprised of samples collected from unlearned configurations, which was employed to further evaluate the feasibility and robustness of the proposed approach. To provide a comparative analysis of the enhanced sensitivity of the temperature anti-principal mode, another set of datasets was constructed following the same procedure, with the unmodulated wavefront as the illuminating light.

Prior to training the model, preprocessing of the samples contained in the dataset is required. The collected speckle patterns are cropped into a 100×100 pixels window centered on the speckle, and then downsampled to 32×32 pixels. To reduce the computational complexity, principal component analysis (PCA) was employed to reduce the dimensionality of the samples. PCA is the most commonly used data dimensionality reduction algorithm, which can improve the learning efficiency and convergence speed of the model while preserving the abstract features of the samples as much as possible. However, in practical applications, it is necessary to carefully

choose the dimensionality of the low-dimensional space, ensuring a balance between convergence speed and model accuracy. In this work, contribution rate is defined as the amount of data preserved in the direction of the principal component, while the cumulative contribution rate is defined as the ratio between the features contained in the low-dimensional space and those contained in the original space. As shown in Fig. 6, when the dimension is 20, the low-dimensional space contains 99.9% of the original data features. Therefore, in this work, the dimension of the low-dimensional space was chosen to be 20.

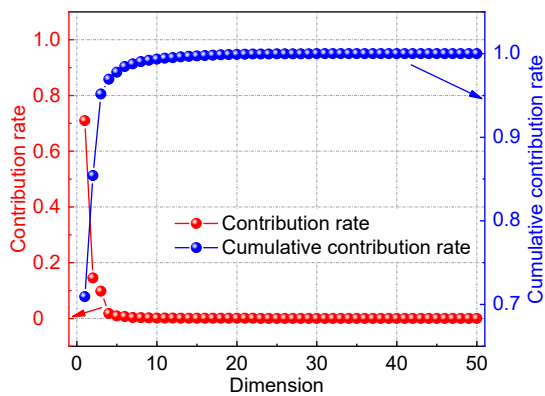


**Fig. 6 | The contribution rate and cumulative contribution rate of principal components under different dimensions.**

The training and validation of the model were conducted on a computer equipped with an i7-10857H CPU. The architecture of the back propagation (BP) neural network used in this work is 20-15-1, indicating that the number of neurons in the input layer, hidden layer, and output layer is 20, 15, and 1, respectively. The number of neurons in the input layer is equivalent to the dimensionality of the optimized feature space obtained via PCA algorithm. The number of neurons in the hidden layer is typically determined empirically based on the number of input and output layer neurons, and subsequently adjusted based on the training process. The PCA algorithm was used to perform data dimensionality reduction on all samples in the dataset, which took approximately 2 seconds. Subsequently, the BP neural network was trained on the preprocessed training set A for 1.1 seconds, with an initial learning rate of 0.01. To mitigate the uncertainty caused by sensitivity to initial values, a transfer learning approach was adopted. Specifically, weights from similar models trained in other speckle pattern demodulation works were extracted and used to initialize the model in this work. As a first step, the prediction accuracy of the trained model for the learned configurations

was tested when illuminated with unmodulated wavefront and temperature anti-principal mode, respectively. The demodulation speed of the trained model is 0.007 milliseconds per frame. The testing results are depicted in Fig. 7, where Fig. 7(a) and 7(b) illustrate the prediction errors and error distribution histogram for the fiber specklegram temperature sensor illuminated with the unmodulated wavefront. Similarly, Fig. 7(c) and 7(d) show the corresponding results for the sensor with enhanced sensitivity using the temperature anti-principal mode. For the learned configurations, the average prediction errors of the fiber specklegram temperature sensor with temperature anti-principal mode and unmodulated wavefront are 0.01 °C and 0.018 °C, respectively. Based on the comparison of results, it can be observed that the fiber speckle pattern temperature sensor with enhanced sensitivity using the temperature anti-principal mode exhibits slightly better sensing accuracy than the one using the unmodulated wavefront.

In fact, it is impossible for the dataset to encompass all possible configurations, hence the generalization ability of the deep learning model towards unseen or unlearned configurations determines its applicability and feasibility. Testing set B includes samples collected from configurations that the model has not learned, which can be further utilized to evaluate the predictive accuracy of the trained model. Figure 8 illustrates the testing results for the unlearned configurations, with Fig. 8(a, b) displaying the prediction errors and error distribution histogram for the fiber specklegram temperature sensor with the unmodulated wavefront, and Fig. 8(c, d) presenting the corresponding results for the sensor with enhanced sensitivity through the temperature anti-principal mode. The fiber specklegram temperature sensor with temperature anti-principal mode and unmodulated wavefront achieved average prediction errors of 0.12 °C and 0.84 °C, respectively, for unlearned configurations. From Fig. 8(a, b), it can be observed that the fiber specklegram temperature sensor with unmodulated wavefront exhibits poor generalization performance for unlearned configurations, with a prediction error range of  $\pm 2$  °C. The observed phenomenon can be attributed to the fact that the unmodulated wavefront is less sensitive to temperature-induced distortions. Consequently, when the external temperature changes, the fluctuation in the field distribution at the output end of the fiber is relatively small.

The confusion in the deep learning model arises from its difficulty in distinguishing the speckle pattern



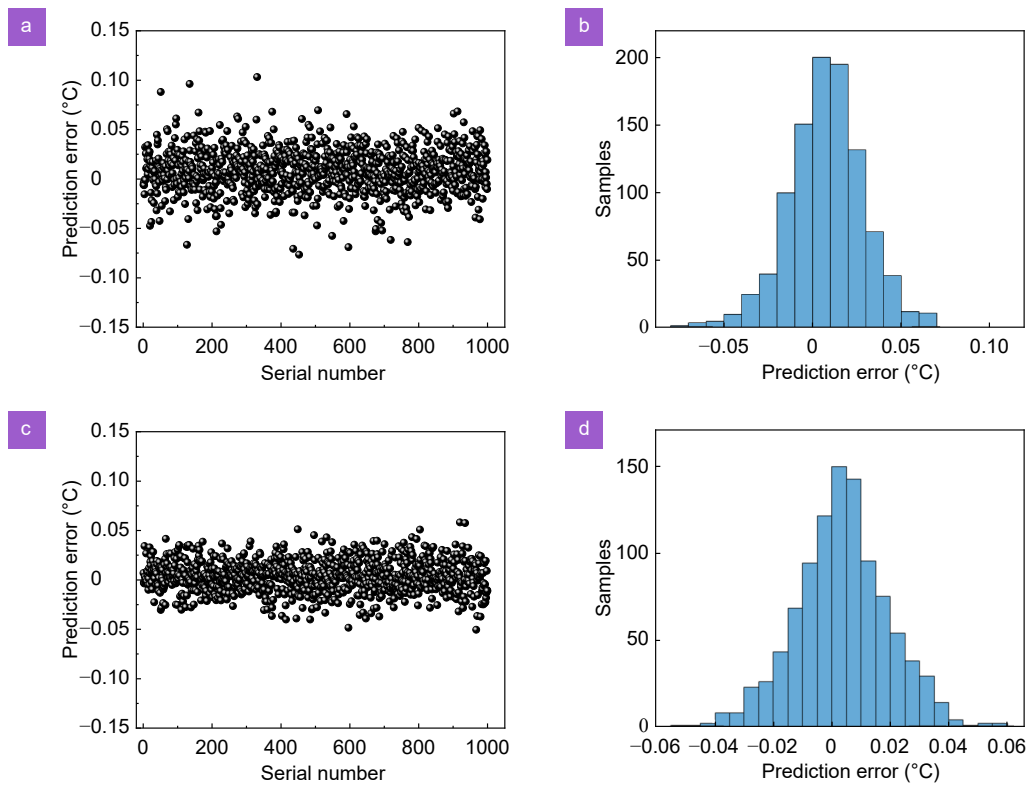


**Fig. 7 | The trained deep learning model is used to predict learned configurations. (a, b)** Prediction error and error distribution histogram of a fiber specklegram temperature sensor with unmodulated wavefront. **(c, d)** The prediction error and error distribution histogram of the fiber specklegram temperature sensor sensitized by the temperature anti-principal mode.

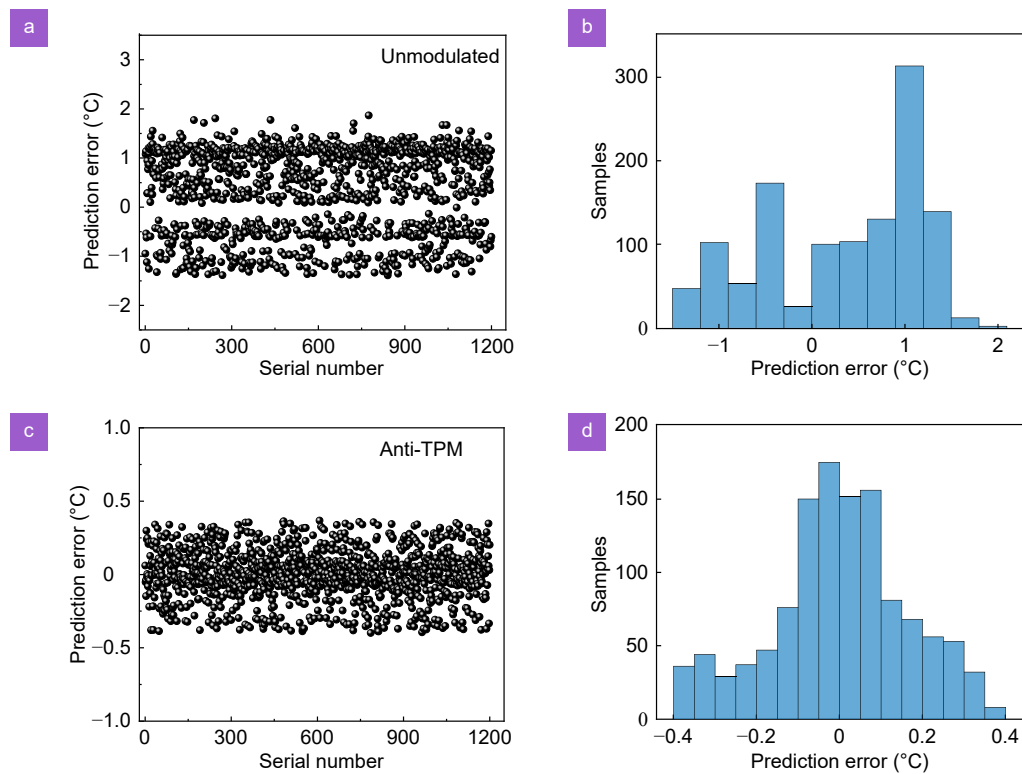


**Fig. 8 | The trained deep learning model is used to predict unlearned configurations. (a, b)** Prediction error and error distribution histogram of a fiber specklegram temperature sensor with unmodulated wavefront. **(c, d)** The prediction error and error distribution histogram of the fiber specklegram temperature sensor sensitized by the temperature anti-principal mode.

changes caused by small temperature fluctuations under unmodulated wavefront illumination. Therefore, the fiber specklegram temperature sensor with unmodulated wavefront has limited resolution. In contrast, fiber specklegram temperature sensors with enhanced sensitivity using temperature anti-principal mode exhibit remarkable superiority for unlearned configurations, with an error range of  $\pm 0.4$  °C and most errors concentrated around 0 °C. Fiber specklegram temperature sensors with temperature anti-principal mode sensitization demonstrate outstanding advantages in prediction accuracy, resolution, and stability. This is because the temperature anti-principal mode scheme can enhance the response of optical fiber to temperature-induced distortion, leading to significant fluctuations in the field distribution at the far end of the optical fiber with temperature changes. This makes it easier for deep learning models to distinguish changes in the speckle pattern caused by small temperature fluctuations.

For a comprehensive analysis, the performance of the fiber specklegram temperature sensor based on temperature principal modes was investigated, as depicted in Fig. 9. Figure 9(a) and 9(b) illustrate the prediction errors and error distribution histograms for the learned configurations, while Fig. 9(c) and 9(d) depict those for the unlearned configurations. The average prediction errors for the learned configurations and unlearned configurations are 0.30 °C and 1.42 °C, respectively. As previously mentioned, temperature principal modes can notably suppress the response of the output field to temperature fluctuations, leading to a significantly inferior performance of sensors based on temperature principal modes compared to the two sensors discussed earlier.

To have a clearer understanding about the features of the previously proposed fiber specklegram temperature sensor based on regression neural network, a comparison is shown in Table 1. It is evident that compared to sensitivity enhancement methods reported based on sensing structure optimization, the approach proposed in this work, utilizing wavefront shaping, can effectively enhance the sensitivity to a greater extent. It is important to note that the method proposed in this work demonstrates high compatibility, seamlessly integrating with sensing structure optimization techniques, and holds promise for further enhancing the performance.

## Discussion

In this work, we extend the concept of principal modes

beyond frequency, presenting and experimentally generating temperature principal modes and temperature anti-principal modes for the first time. The temperature principal mode exhibits good resistance to temperature-induced distortion, while the temperature anti-principal mode has a narrower temperature bandwidth than the unmodulated wavefront. The normalized bandwidths of the temperature principal mode and temperature anti-principal mode are maintained at around 1.4 and 0.67, respectively. Without compromising the structural integrity of the fiber and without resorting to thermosensitive materials, we have effectively manipulated the temperature response within MMF solely through wavefront shaping techniques. Furthermore, the generation of temperature principal modes and temperature anti-principal modes has been demonstrated to be highly convenient, relying solely on multi-temperature transmission matrix and generalized Wigner-Smith operator. In this study, incomplete transmission matrices are used to generate temperature principal modes and temperature anti-principal modes. It can be observed from both the experimental results and previously reported works<sup>35,36</sup> that despite their incompleteness, these transmission matrices still manage to accurately describe the transmission characteristics of multimode fibers and successfully generate the exact Wigner-Smith operator.

Temperature-induced distortion is an issue that cannot be overlooked in engineering based on optical fiber speckle patterns. In such circumstances, the temperature principal modes stand out as a promising option, offering the capability to manipulate the temperature response within the MMF conveniently while preserving the structural integrity of the fiber. The temperature principal mode can suppress distortion induced by temperature fluctuations, yielding an output light field with minimal temperature sensitivity, making it highly promising for applications such as fiber optic spectrometers<sup>51</sup>, fiber optic imaging<sup>52</sup>, and fiber optic specklegram sensors<sup>48</sup>. In fiber-optic imaging, both the reconstruction algorithms based on the transmission matrix and those based on deep learning rely on the mapping relationship between the speckle pattern and the target image. The distortion induced by temperature can introduce additional perturbations, posing challenges for high-resolution reconstruction of the target image. Various methods have been reported to mitigate temperature-induced distortions, such as in learning-based fiber imaging schemes where distortion can be alleviated by

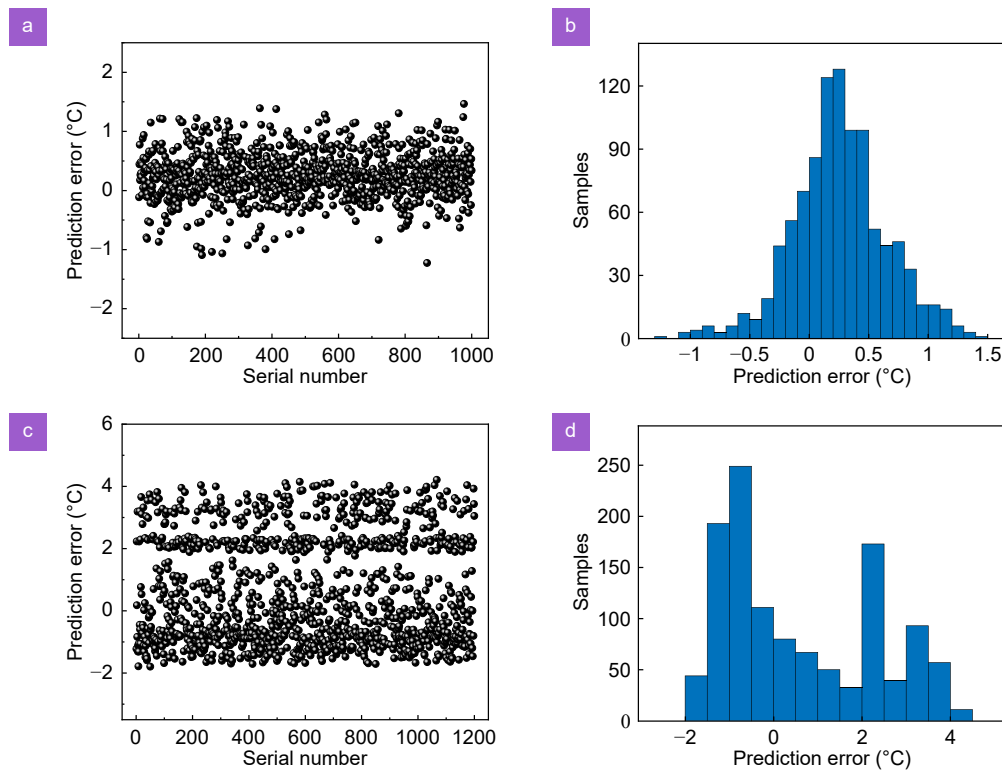


**Fig. 9 | The performance of fiber specklegram temperature sensors based on temperature principal modes. (a, b) Prediction errors and error distribution histograms for learned configurations. (c, d) Prediction errors and error distribution histograms for unlearned configurations.**

**Table 1 | Objective evaluation parameters of the different transform domain fusion methods.**

Model	Sensitization method	Measurement error	
		Learned samples (°C)	Unlearned samples (°C)
CNN <sup>49</sup>	Side-polished	0.34	/
VGG <sup>50</sup>	Exposed core	0.14	0.2
MLP <sup>50</sup>	Exposed core	0.079	0.39
This work	Wavefront shaping	0.01	0.12

expanding the dataset, albeit at the cost of additional time and experimental efforts<sup>52</sup>. In this work, the temperature-principal mode described can effectively alleviate the fluctuations in the spatial distribution of the output field caused by temperature-induced distortion, providing potential for more convenient and cost-effective improvement of imaging quality. Although the optimization problem will undoubtedly become more intricate, we remain optimistic that by researching and developing more efficient and tailored optimization algorithms, and refining the calibration strategy of the temperature principal mode, these challenges can be effectively surmounted. In the field of optical fiber sensing, fiber specklegram sensors have gained significant attention owing to their cost-effective sensing scheme and streamlined fabrication process. The efficacy of this sensor in demodulating sensing signals hinges upon the accuracy of the

fitting relationship between the speckle pattern and the sensing parameter. Nevertheless, when measuring sensing parameters beyond temperature, the distortion induced by temperature changes can engender a noteworthy reduction in the demodulation accuracy, thereby leading to significant uncertainties in the measurement process. While conducting a detailed analysis of the correlation between the speckle pattern and the measured parameter in various temperature scenarios can alleviate the distortions, it entails a substantial investment of time and effort<sup>52</sup>. The utilization of temperature principal modes offers an effective approach to mitigate the distortion effects caused by temperature variations, thereby increasing the sensitivity of the sensor without compromising its structural integrity.

Contrary to the temperature principal mode, the temperature anti-principal modes are a unique set of optical

channels characterized by their heightened sensitivity to distortions induced by temperature fluctuations. The optimization strategy described earlier allows us to generate such highly sensitive state by just maximizing the functional in Eq. (3). Compared to unmodulated wavefronts like Gaussian beams, the output field of the temperature anti-principal mode exhibits faster decorrelation when the environmental temperature changes—a property that holds promise for sensing applications with MMFs. The design scheme of this learning-empowered fiber specklegram temperature sensor based on temperature anti-principal mode sensitization can be divided into several steps: Initially, calibrate the multi-temperature transmission matrix and generalized Wigner-Smith operator to subsequently excite the temperature anti-principal mode. Next, gather speckle patterns at the distal end of the fiber under different temperatures and compile the dataset. Finally, the deep learning model is employed to learn the mapping relationship between speckle patterns and temperature fluctuations on the dataset, utilizing the trained model to demodulate the sensing signal. This proposed approach introduces a new avenue for sensor sensitization, offering a convenient and effective means to enhance the sensor's response to temperature fluctuations solely through wavefront shaping techniques without compromising the fiber structure. Importantly, this method is compatible with commonly used sensor sensitization methods based on thermosensitive materials or complex sensing structures.

The generation of temperature principal and anti-principal modes is solely dependent on the transmission matrices calibrated at different temperatures and the generalized Wigner-Smith operator, regardless of the type of fiber and the wavelength of the incident light. Therefore, our methodology, which involves the concepts of temperature principal mode and temperature anti-principal mode, as well as the ability to create complex fields through wavefront shaping, is not confined to any particular types of scattering systems or waveforms. We anticipate that our findings can be easily transferred to other experimental platforms or other complex media. It is noted that the original definition of the Wigner-Smith operator is dependent on the scattering matrix<sup>35</sup>, which comprises both transmission and reflection. Therefore, we anticipate no barriers in transferring the concept of temperature principal mode or temperature anti-principal mode to other disordered media with reflection and loss<sup>36</sup>. Additionally, this approach also has

the potential to be generalized as a universal model for exploring more novel light states.

In practical applications, generating temperature principal modes and temperature anti-principal modes in relatively longer fibers (for example, up to 1 km) presents challenges. When transmitting optical signals through a 1 km long MMF, the speckle intensity at the distal end of the fiber will change rapidly with time, even if the proximal input remains constant. This can be attributed to fluctuations of the vibration or airflow over the optical setup that induce slight perturbations on the fiber that become significant over its 1 km length. This perturbation leads to changes in the transmission matrix of the fiber, rendering the principal modes generated based on the original transmission matrix unsuitable for the perturbed fiber. Fortunately, research indicates that these perturbations are not entirely random and can be learned by models such as neural networks. Hence, we are optimistic about successfully generating temperature principal modes and anti-principal modes in relatively longer fibers.

The main sources of error in our work are attributed to the errors during transmission matrix calibration, imperfections in the optimization strategy, and the incompleteness of the transmission matrix. Our future work will focus on several aspects of improvement. The initial step involves further optimization of the experimental setup to reduce potential sources of systematic error. Subsequently, advanced optimization techniques, which are more efficient, problem-specific, and have better performance, are investigated to enhance temperature bandwidth. Finally, employing the more comprehensive multi-temperature vector transmission matrix<sup>53</sup> or multi-temperature polarization transmission matrix<sup>10</sup> to generate temperature principal modes and temperature anti-principal modes with improved performance.

## Conclusion

In summary, we have discovered a set of distinctive light states in multimode fibers that exhibit either enhanced robustness or heightened sensitivity to temperature-induced distortion compared to the unmodulated wavefronts. These states can be referred to as the temperature principal mode and temperature anti-principal mode, and can be generated based on experimentally-measured multi-temperature transmission matrices. The temperature principal mode can robustly increase the temperature bandwidth by approximately 40%, while the



temperature anti-principal mode can reduce the temperature bandwidth to 67% of the unmodulated wavefront. To fully leverage the characteristics of the temperature anti-principal mode, a learning-empowered fiber specklegram temperature sensor based on temperature anti-principal mode sensitization is proposed. This sensor exhibits superior performance in both resolution and sensitivity compared to traditional solutions, and can be easily implemented without compromising the robustness of the fiber structure. Our method has potential applications in optical communication, imaging, and sensing, and can be easily extended to other multimode waveguides, providing an inspiring reference for exploring more novel states.

## References

- Randel S, Ryf R, Sierra A et al. 6×56-Gb/s mode-division multiplexed transmission over 33-km few-mode fiber enabled by 6×6 MIMO equalization. *Opt Express* **19**, 16697–16707 (2011).
- Carpenter J, Thomsen BC, Wilkinson TD. Degenerate mode-group division multiplexing. *J Lightwave Technol* **30**, 3946–3952 (2012).
- Carpenter J, Wilkinson TD. All optical mode-multiplexing using holography and multimode fiber couplers. *J Lightwave Technol* **30**, 1978–1984 (2012).
- Kahn JM, Miller DAB. Communications expands its space. *Nat Photonics* **11**, 5–8 (2017).
- Richardson DJ, Fini JM, Nelson LE. Space-division multiplexing in optical fibres. *Nat Photonics* **7**, 354–362 (2013).
- Borhani N, Kakkava E, Moser C et al. Learning to see through multimode fibers. *Optica* **5**, 960–966 (2018).
- Marima D, Hadad B, Froim S et al. Visual data detection through side-scattering in a multimode optical fiber. *Opt Lett* **45**, 6724–6727 (2020).
- Zhang LH, Xu RC, Ye HL et al. High definition images transmission through single multimode fiber using deep learning and simulation speckles. *Opt Lasers Eng* **140**, 106531 (2021).
- Zhao J, Sun YY, Zhu HB et al. Deep-learning cell imaging through Anderson localizing optical fiber. *Adv Photonics* **1**, 066001 (2019).
- Fan WR, Chen ZY, Yakovlev VV et al. High-fidelity image reconstruction through multimode fiber via polarization-enhanced parametric speckle imaging. *Laser Photonics Rev* **15**, 2000376 (2021).
- Gao H, Hu HF, Zhao Y et al. Highly-sensitive optical fiber temperature sensors based on PDMS/silica hybrid fiber structures. *Sens Actuators A Phys* **284**, 22–27 (2018).
- Gao H, Zhang YX, Zhang WG et al. High sensitivity optical fiber temperature sensor based on PDMS-filled with extended measuring range. *Optik* **248**, 168181 (2021).
- Banerjee A, Mukherjee S, Verma RK et al. Fiber optic sensing of liquid refractive index. *Sens Actuators B Chem* **123**, 594–605 (2007).
- Qin ZG, Qu S, Wang ZQ et al. A fully distributed fiber optic sensor for simultaneous relative humidity and temperature measurement with polyimide-coated polarization maintaining fiber. *Sens Actuators B Chem* **373**, 132699 (2022).
- Wang YK, Tan B, Liu SR et al. An optical fiber-waveguide-fiber platform for ppt level evanescent field-based sensing. *Sens Actuators B Chem* **306**, 127548 (2020).
- Kotov LV, Aleshkina SS, Khudyakov MM et al. High-brightness multimode fiber lasers for resonant pumping. *J Lightwave Technol* **35**, 4540–4546 (2017).
- Zhu X, Schulzgen A, Li H et al. High-power fiber lasers and amplifiers based on multimode interference. *IEEE J Sel Top Quantum Electron* **15**, 71–78 (2009).
- Bai N, Ip E, Wang T et al. Multimode fiber amplifier with tunable modal gain using a reconfigurable multimode pump. *Opt Express* **19**, 16601–16611 (2011).
- Khudyakov MM, Lipatov DS, Gur'yanov AN et al. Highly efficient 3.7 kW peak-power single-frequency combined Er/Er-Yb fiber amplifier. *Opt Lett* **45**, 1782–1785 (2020).
- Popoff SM, Lerosey G, Carminati R et al. Measuring the transmission matrix in optics: an approach to the study and control of light propagation in disordered media. *Phys Rev Lett* **104**, 100601 (2010).
- Carpenter J, Eggleton BJ, Schröder J. Complete spatiotemporal characterization and optical transfer matrix inversion of a 420 mode fiber. *Opt Lett* **41**, 5580–5583 (2016).
- Park J, Park JH, Yu H et al. Focusing through turbid media by polarization modulation. *Opt Lett* **40**, 1667–1670 (2015).
- Gao H, Hu HF, Zhan QW et al. Efficient switchable common path interferometer for transmission matrix characterization of scattering medium. *IEEE Photonics J* **14**, 7825005 (2022).
- Li SH, Horsley SAR, Tyc T et al. Memory effect assisted imaging through multimode optical fibres. *Nat Commun* **12**, 3751 (2021).
- Popoff S, Lerosey G, Fink M et al. Image transmission through an opaque material. *Nat Commun* **1**, 81 (2010).
- Zhao TR, Ourselin S, Vercauteren T et al. Seeing through multimode fibers with real-valued intensity transmission matrices. *Opt Express* **28**, 20978–20991 (2020).
- Choi Y, Yoon C, Kim M et al. Scanner-free and wide-field endoscopic imaging by using a single multimode optical fiber. *Phys Rev Lett* **109**, 203901 (2012).
- Bianchi S, Di Leonardo R. A multi-mode fiber probe for holographic micromanipulation and microscopy. *Lab Chip* **12**, 635–639 (2012).
- Leedumrongwatthanakun S, Innocenti L, Defienne H et al. Programmable linear quantum networks with a multimode fibre. *Nat Photonics* **14**, 139–142 (2019).
- Matthès MW, Bromberg Y, de Rosny J et al. Learning and avoiding disorder in multimode fibers. *Phys Rev X* **11**, 021060 (2021).
- Smith FT. Lifetime matrix in collision theory. *Phys Rev* **118**, 349–356 (1960).
- Wigner EP. Lower limit for the energy derivative of the scattering phase shift. *Phys Rev* **98**, 145–147 (1955).
- Carpenter J, Eggleton BJ, Schröder J. Observation of Eisenbud–Wigner–Smith states as principal modes in multimode fibre. *Nat Photonics* **9**, 751–757 (2015).
- Xiong W, Ambichl P, Bromberg Y et al. Principal modes in multimode fibers: exploring the crossover from weak to strong mode coupling. *Opt Express* **25**, 2709–2724 (2017).
- Xiong W, Ambichl P, Bromberg Y et al. Spatiotemporal control of light transmission through a multimode fiber with strong mode

- coupling. *Phys Rev Lett* **117**, 053901 (2016).
36. Ambichl P, Xiong W, Bromberg Y et al. Super- and anti-principal-modes in multimode waveguides. *Phys Rev X* **7**, 041053 (2017).
  37. Arrizón V, Ruiz U, Carrada R et al. Pixelated phase computer holograms for the accurate encoding of scalar complex fields. *J Opt Soc Am A* **24**, 3500–3507 (2007).
  38. Zhang YL, Suo JL, Wang YW et al. Doubling the pixel count limitation of single-pixel imaging via sinusoidal amplitude modulation. *Opt Express* **26**, 6929–6942 (2018).
  39. Li SH, Saunders C, Lum DJ et al. Compressively sampling the optical transmission matrix of a multimode fibre. *Light Sci Appl* **10**, 88 (2021).
  40. Fujiwara E, da Silva LE, Cabral TD et al. Optical fiber specklegram chemical sensor based on a concatenated multimode fiber structure. *J Lightwave Technol* **37**, 5041–5047 (2019).
  41. Chen YF, Hu YC, Yan F et al. Ultrahigh-sensitive and compact temperature sensor based on no-core fiber with PMMA coating. *Opt Express* **29**, 37591–37601 (2021).
  42. Du C, Wang Q, Zhao Y. Electrically tunable long period gratings temperature sensor based on liquid crystal infiltrated photonic crystal fibers. *Sens Actuators A Phys* **278**, 78–84 (2018).
  43. Xue JJ, Zhang YX, Liu W et al. Ultrahigh-sensitivity SPR fiber temperature sensor based Ge<sub>2</sub>Sb<sub>2</sub>Te<sub>5</sub> and cyclohexane. *Sens Actuators A Phys* **345**, 113786 (2022).
  44. Cheng S, Hu WB, Ye HR et al. Tapered multicore fiber interferometer for ultra-sensitive temperature sensing with thermo-optical materials. *Opt Express* **29**, 35765–35775 (2021).
  45. Yue CX, Ding H, Ding W et al. Weakly-coupled multicore optical fiber taper-based high-temperature sensor. *Sens Actuators A Phys* **280**, 139–144 (2018).
  46. Feng F, Chen W, Chen DH et al. In-situ ultrasensitive label-free DNA hybridization detection using optical fiber specklegram. *Sens Actuators B Chem* **272**, 160–165 (2018).
  47. Etchepareborda P, Federico A, Kaufmann GH. Sensitivity evaluation of dynamic speckle activity measurements using clustering methods. *Appl Opt* **49**, 3753–3761 (2010).
  48. Gao H, Hu HF. Spatially-resolved bending recognition based on a learning-empowered fiber specklegram sensor. *Opt Express* **31**, 7671–7683 (2023).
  49. Lu S, Tan ZW, Ji WJ et al. A spatial domain multiplexing technology for fiber specklegram sensor. *Opt Fiber Technol* **81**, 103505 (2023).
  50. Smith DL, Nguyen LV, Ottaway DJ et al. Machine learning for sensing with a multimode exposed core fiber specklegram sensor. *Opt Express* **30**, 10443–10455 (2022).
  51. Redding B, Popoff SM, Cao H. All-fiber spectrometer based on speckle pattern reconstruction. *Opt Express* **21**, 6584–6600 (2013).
  52. Bagley N, Kremp T, Lamb ES et al. Transfer learning and generalization of a neural-network-based multimode fiber position and imaging sensor under thermal perturbations. *Opt Fiber Technol* **70**, 102855 (2022).
  53. Tripathi S, Paxman R, Bifano T et al. Vector transmission matrix for the polarization behavior of light propagation in highly scattering media. *Opt Express* **20**, 16067–16076 (2012).

## Acknowledgements

We are grateful for financial supports from the National Natural Science Foundation of China (62075132 and 92050202), Natural Science Foundation of Shanghai (22ZR1443100).

## Author contributions

HF Hu proposed the original idea. H Gao fabricated the samples and performed the measurements. QW Zhan supervised the project.

## Competing interests

The authors declare no competing financial interests.



Scan for Article PDF